Journal of Power Sources 450 (2020) 227667

Contents lists available at ScienceDirect

Journal of Power Sources

journal homepage: www.elsevier.com/locate/jpowsour

Multiphysics coupled computational model for commercialized Si/graphite composite anode

Binghe Liu [a,b,c], Yikai Jia [d,e], Jiani Li [a,b], Hanqing Jiang [f], Sha Yin [a,b], Jun Xu [d,e,*]

[a] Vehicle Energy & Safety Laboratory (VESL), Beihang University, Beijing, 100191, China
[b] Department of Automotive Engineering, School of Transportation Science and Engineering, Beihang University, Beijing, 100191, China
[c] Key Laboratory of Impact and Safety Engineering, Ministry of Education, Ningbo University, Ningbo, 315211, China
[d] Department of Mechanical Engineering and Engineering Science, The University of North Carolina at Charlotte, Charlotte, NC, 28223, USA
[e] Vehicle Energy & Safety Laboratory (VESL), North Carolina Motorsports and Automotive Research Center, The University of North Carolina at Charlotte, Charlotte, NC, 28223, USA
[f] School for Engineering of Matter, Transport and Energy, Arizona State University, Tempe, AZ, 85287, USA

HIGHLIGHTS

- A multiphysics model to study LIB with Si/G composite anode is established.
- The model is fully validated by mechanics-electrochemical coupled experiments.
- The model enables a detailed description of both the cell and particle behavior.
- Design-oriented governing factors are systematically discussed.

GRAPHICAL ABSTRACT

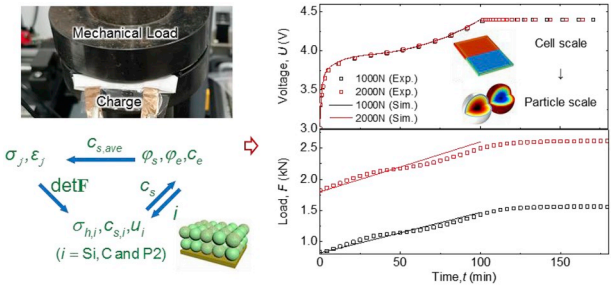

ARTICLE INFO

Keywords:
Si/graphite composite anode
Multiphysics coupling
Modeling
Deformation

ABSTRACT

Si/graphite composite (Si/G) anodes are now regarded among the most commercially available next-generation anode materials. The development of a fully coupled mechanical-electrochemical model for Si/G anode is an essential tool to design safer and lightweight lithium-ion battery modules/packs. In this paper, we establish an efficient model to study lithium-ion battery (LIB) with Si/G composite anode through the coupling of stress-induced battery model and homogenized mechanical model. By designing strategies for the coupling of mechanical and electrochemical governing equations, a multiphysics model is proposed. Experiments for battery charging with simultaneous various mechanical loadings are conducted to validate the established model. Finally, design-oriented parametric studies for governing factors (e.g., the Si/G mixture ratio and battery size) are discussed. Results provide a fundamental understanding of the failure mechanism of the composite anode and offer a powerful design tool for Si/G composite anode design for better electrochemical performance.

* Corresponding author. Department of Mechanical Engineering and Engineering Science, The University of North Carolina at Charlotte, Charlotte, NC, 28223, USA.
E-mail address: jun.xu@uncc.edu (J. Xu).

https://doi.org/10.1016/j.jpowsour.2019.227667
Received 30 October 2019; Received in revised form 16 December 2019; Accepted 26 December 2019

Nomenclature

a_s	active surface area per unit electrode volume
c_s	Li concentration in solid phase
$\widehat{c}_s$	test function related to c_s
c_e	Li^+ concentration in electrolyte
D_s	Diffusion coefficient in solid phase
D_e	Diffusion coefficient in the electrolyte
det **F**	deformation gradient
det$\mathbf{F}_e$	deformation gradient of the elastic deformation
det$\mathbf{F}_d$	deformation gradient of diffusion induced deformation
E	Young's modulus
E_{ref}	open-circuit potential
F	Faraday's constant
i	intercalation reaction current density
$\mathbf{i}_e$	the current density in the liquid phase
i_0	exchange current density
$\mathbf{j}_e$	Li^+ flux density in the electrolyte
$\mathbf{j}_s$	Li flux density in the solid phase
j_s	Li flux density in the solid phase
L	thickness
R	gas constant
R_b	bulk resistance
R_{sei}	resistance of the solid electrolyte interface
R_{ct}	charge-transfer resistance
S_{1D}	section area of 1D battery model
r	radius distance
r_p	particle radius
T	temperature
t_+	transfer data
V	initial volume
ΔV	volume change
ΔV_d	volume change caused by diffusion induced deformation
α	coefficient of lithiation expansion
α_a	anodic transfer coefficient
α_c	cathodic transfer coefficient
β	cathodic symmetry factor
ε_s	volume fraction of the solid phase
ε_e	volume fraction of the electrolyte
ε	strain
η	overpotential
κ_s	electric conductivity in solid phase
κ_e	electric conductivity in electrolyte
σ	stress
σ_h	hydrostatic stress
$\sigma_{h,e}$	hydrostatic stress caused by elastic deformation
$\sigma_{h,d}$	hydrostatic stress caused by diffusion induced stress
ϕ_s	potential in the solid
ϕ_e	potential in the electrolyte
$\mu(c_s)$	concentration-dependent chemical potential
$\gamma_{Si/P1}$	Ratio of solid volume of Si to that of particle P1
γ_{Si}	Si ratio
γ_{P1}	P1 ratio
Ω	the partial molar volume
$1+\frac{d\ \ln f_{\pm}}{d\ \ln c_e}$	molar activity coefficient

The superscript

an	anode
ca	cathode
C	carbon (graphite)
cas	battery casing
eff	effective
max	maximum
surf	surface
sep	separator
ref	reference
Si	silicon
P1	Particle 1 (Si/G composite core-shell particle)
P2	Particle 2 (pure graphite particle)

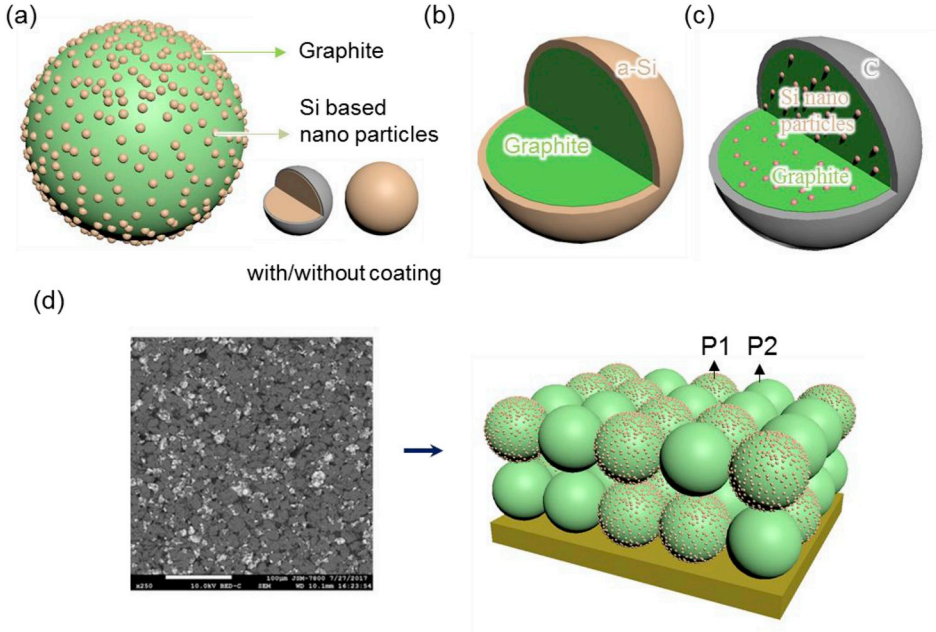

Fig. 1. The structure of (a) graphite with coating Si-based nano-particles, (b) graphite with coating atmosphere-Si and (c) flack graphite with mixed Si-based nano-particles. (d) SEM picture and schematic diagram of the anode composed of P1 and P2 [27].

Table 1
Governing equations of P2D model adopted in this paper.

Equation name	Equations	No.
Butler–Volmer equation	$i = i_0\left\{\exp\left[\frac{(1-\beta)F\eta}{RT}\right] - \exp\left(-\frac{\beta F\eta}{RT}\right)\right\}$	(1)
Exchange current density	$i_0 = Fk_c^{\alpha_a}k_a^{\alpha_c}(c_{s,\max} - c_{s,surf})^{\alpha_c}(c_{s,surf})^{\alpha_c}\left(\frac{c_e}{c_{c,ref}}\right)^{\alpha_a}$	(2)
Overpotential	$\eta = \phi_s - \phi_e - E_{ref}(c_{s,surf})$	(3)
Conservation of charge	$\nabla\cdot\mathbf{i}_s = -a_s i$ and $\nabla\cdot\mathbf{i}_e = a_s i$	(4)
Conservation of mass	$\varepsilon_e\frac{\partial c_e}{\partial t} = -\nabla\cdot\mathbf{j}_e + \frac{a_s i}{F}$	(5)
Active surface area	$a_s = \frac{3\varepsilon_s}{r_p}$	(6)
Current density in the liquid phase	$\mathbf{i}_e = -\kappa_{e,eff}\left[\nabla\phi_e - \frac{2RT}{F}\left(1 + \frac{d\ln f_+}{d\ln c_e}\right)(1-t_+)\nabla\ln c_e\right]$	(7)
Current density in solid phase	$\mathbf{i}_s = -\kappa_{s,eff}\nabla\phi_s$	(8)
Li^+ flux density in liquid phase	$\mathbf{j}_e = -D_{e,eff}\nabla c_e + \frac{t_+}{F}\mathbf{i}_e$	(9)
Conservation of Li in the particle	$\frac{\partial c_s}{\partial t} + \frac{\partial \mathbf{j}_s}{\partial \mathbf{x}} = 0$	(10)

1. Introduction

High energy density demand for lithium-ion battery (LIB) powered electric vehicles requires new anode materials. By taking advantage of both high theoretical capacity and limited deformation during the charging/discharging cycles, Si/graphite (Si/G) composite anode emerges as one of the most promising next-generation anode materials commercial wise [1]. However, relatively large deformation (compared to pure graphite), possible deterioration during cycles, and an increasingly stringent requirement for battery safety call for a fundamental understanding of the multiphysics behaviors of Si/G where mechanics, electrochemistry, irreversible thermodynamics and transport phenomena are strongly and nonlinearly coupled.

From a mechanical point of view, detailed model of a LIB cell by considering anode, cathode separator, and battery casing has been developed to describe the mechanical deformation of each component material subjected to various external mechanical loadings [2]. On the other hand, for more efficient computation, a homogenized method was smartly adopted to describe the jellyroll deformation behaviors [3–6]. Complicated mechanical behavior such as anisotropicity, strain rate effect as well as SOC effect over the mechanical behavior, which stems from the specific materials and structures of jellyroll, were also included within the mechanical model, serving as a first step to tentatively describe the multiphysics behaviors [3]. Further, these mechanical models were included within the multiphysics framework to predict cell behaviors under mechanical abusive loading [7–9]. From an electrochemical point of view, the pseudo-2D model (P2D), single particle model, and porous electrode model with the polynomial approximation (PP) were the most widely used models to predict the electrochemical behavior [10–12]. The coupling of mechanical effect within the electrochemical model was used to describe Li diffusion equations [13–16] by relevant physical variables (e.g., diffusion coefficient) [17–19], open-circuit potential model [20] and Butler–Volmer equation [21].

Thanks to recent progress on battery coupling modeling, coupling strategies of electrochemistry and mechanics are now available for various length scales. In micro-scale (i.e., particle scale, from 100 nm to 10 μm), a two-way coupling model between diffusion and stress was developed [16,17]. The anisotropic [22], deformation [16], phase-separation [23,24], cracks [25,26] and contract stress between particles [27] can be studied using these micro-scale models. In meso-scale (i.e. electrolyte scale, from 100 μm to 1 mm), reconstructed microstructures [28,29] and homogenization method [20,30,31] were both employed to study the stress and deformation related multiphysics behavior of the components in LIBs. In the macro-scale (i.e. cell-pack scale 1 mm – 1m), a phenomenological model was established to predict the bulk deformation of LIB during charging [32].

Nevertheless, previous coupling models are not capable of describing either the particular structure of the Si/G anode or the coupling behavior in multiscale simultaneously, offering limited design guidance for further development for Si/G composite anode. In this study, we present a multiphysics-based model to study LIB with Si/G composite anode through the coupling of stress-induced battery model and homogenized mechanical model. This model enables a detailed description of both the cell structure and particle behavior with consideration of stress-induced deformation and electrochemistry. This paper is organized as follows. In Section 2, we first define the target problem followed by modeling framework and coupling methodology. Also, experiment methodologies are introduced in detail. In Section 3, typical results from the model are presented and validated by experiments. In Section 4, governing designing factors are systematically discussed. Finally, conclusions are summarized in Section 5.

Table 2
The basic information of the commercial pouch cell.

Terms	Value/Information
Sizes	84 mm × 64 mm × 3.4 mm
Weight	46 g
Rated capacity	3240 mAh
Typical capacity	3340 mAh
Rated voltage	3.82 V
Limited charge voltage	4.4 V

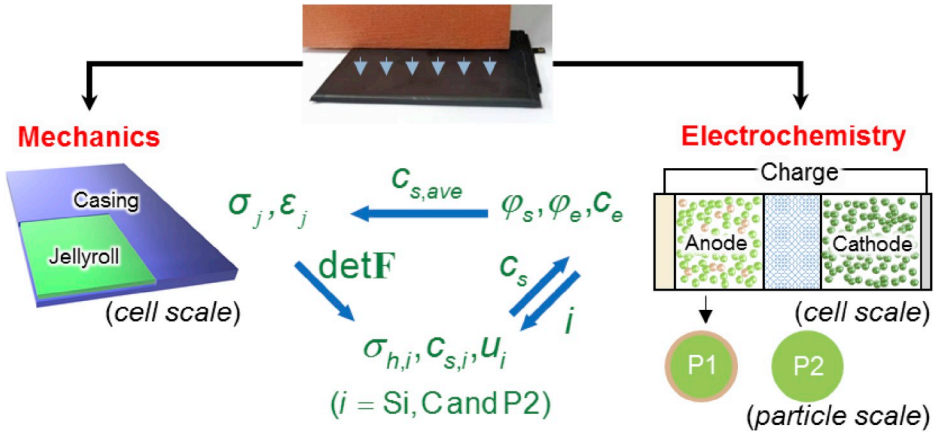

Fig. 2. Schematics of the coupling method of the stress-induced battery model and mechanical model.

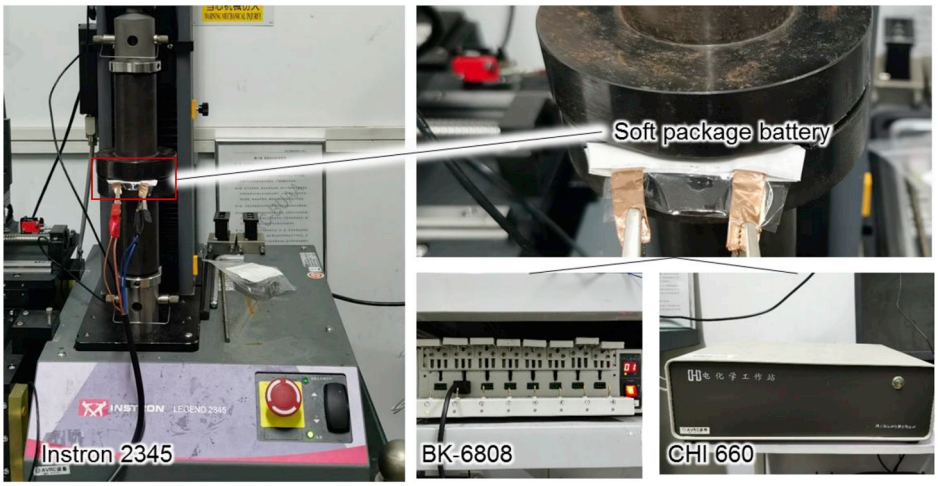

Fig. 3. The instruments and setups of the charging and EIS experiment under mechanical loading.

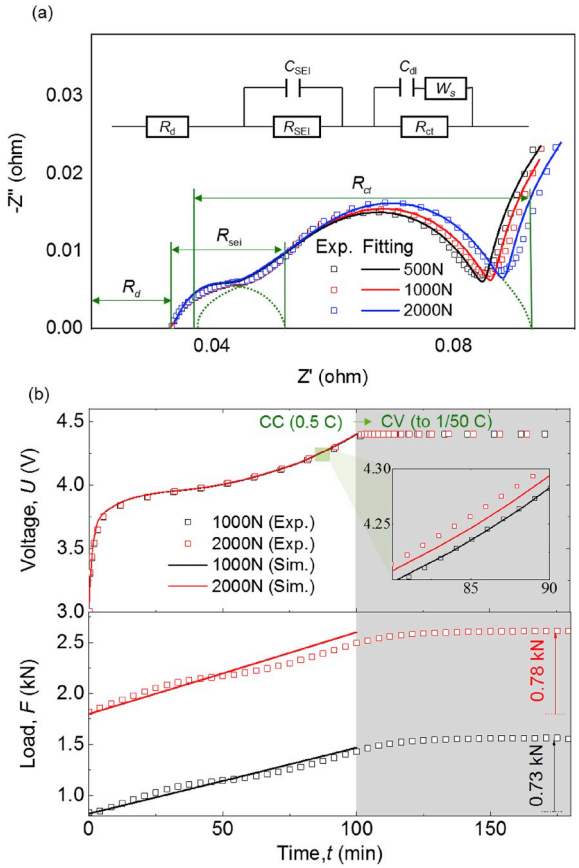

Fig. 4. The electrochemical operations at different loading conditions: (a) EIS experiments and (b) charging experiments.

2. Methodology

2.1. Problem description

Fig. 1(a)-(c) illustrate three typical structures of the present Si/G composite anode where the first one is graphite coated with Si-based nano-particles [33,34]; the second one is graphite coated with amorphous-Si (a-Si) [35]; and the third case is the flack graphite with mixed Si-based nano-particles [36,37]. These structures can all be regarded as a core-shell type. Further, such core-shell structure particles can further be mixed with pure graphite particles [1,27], shown in Fig. 1 (d).

In this paper, the target anode material is a mixture of core-shell structure and graphite shown in Fig. 1(d). Particle 1 (P1) is the core-shell particle, and Particle 2 (P2) is the pure graphite particle. In this study, the structure of Fig. 1 (a) is chosen as P1 for the core-shell particle.

2.2. Modeling methodology

2.2.1. Stress-induced electrochemical model

The stress-induced battery model is based on the P2D model (the governing equations are summarized in Table 1).

As we discussed above, there are two types of particles (i.e., core-shell structured Si/G and pure graphite) mixed together such that the variables and parameters of the solid phase are differentiated by subscripts for "P1" and "P2", respectively. The volume fraction of the solid phase $\varepsilon_{s,an}$ can be then calculated as

$$\varepsilon_{s,an} = \varepsilon_{s,\mathrm{P1}} + \varepsilon_{s,\mathrm{P2}}, \tag{11}$$

where $\varepsilon_{s,P1}$ and $\varepsilon_{s,P2}$ are the volume fractions for P1 and P2, respectively.

The variables and parameters in the liquid phase are assumed to be the same as those in the anode. If we consider the mechanical stress over electrochemical behavior, the flux $\mathbf{j}_s$ then can be expressed as

$$\mathbf{j}_s = -Mc_s\frac{\partial \mu}{\partial \mathbf{x}}, \tag{12}$$

$$\mu = \mu(c_s) - \Omega\sigma_h, \tag{13}$$

where Ω is the partial molar volume, $\sigma_h = trace(\boldsymbol{\sigma})$ is the hydrostatic stress, $M = \frac{D_0}{RT}\left(1 - \frac{c_s}{c_{s,\max}}\right)$ is the mobility of Li, and $\mu(c_s)$ is the Li concentration-dependent chemical potential (which is related to the open-circuit potentials E_{ref}), written as

$$\mu(c_s) = \mu(Li) - FE_{ref} \tag{14}$$

E_{ref} relates to the stress caused by the elastic deformation $\sigma_{h,e}$ [20] via

$$E_{ref} = E_{ref}(c_s / c_{s,\max}) + \frac{\Omega\sigma_{h,e}}{F} \tag{15}$$

For spherical particles, Eq. (10) can be degraded into a typical spherical symmetry problem as

$$\frac{\partial c_s}{\partial t} + \frac{1}{r^2}\frac{\partial r^2 j_s}{\partial r} = 0 \tag{16}$$

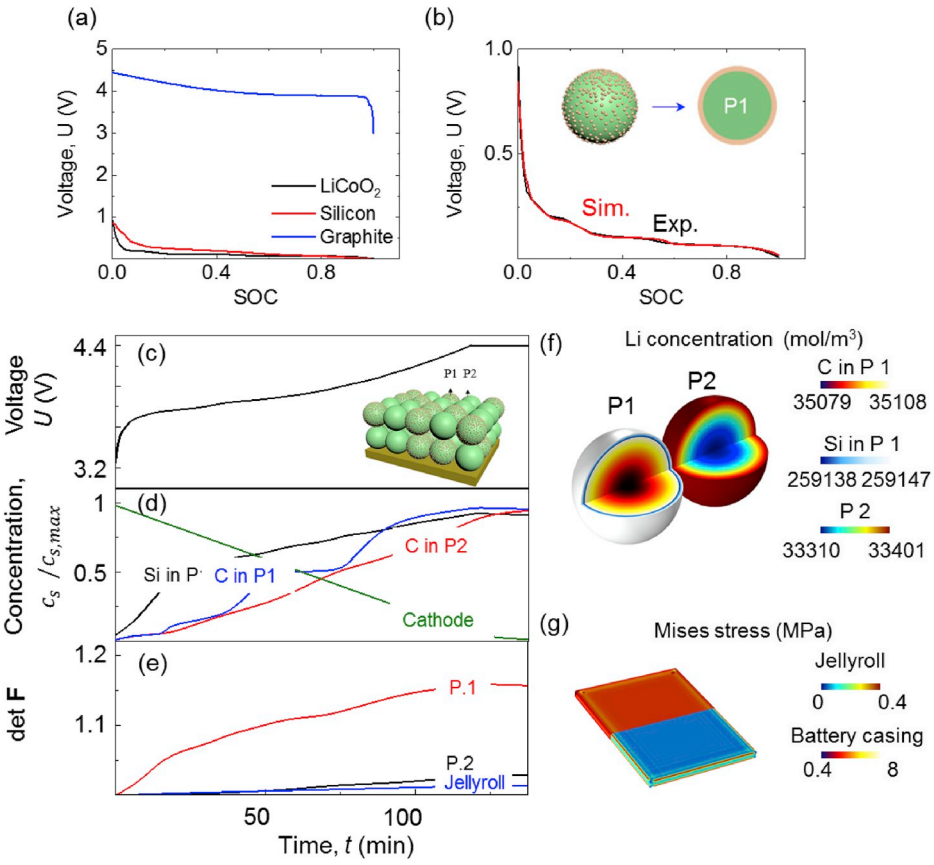

Fig. 5. (a) The open-circuit potential curve of $LiCoO_2$, Si, and graphite. (b) The comparison of the simulation and the half-cell experiment of Ref. [33]. The simulated (c) voltage-time curve, (d) normalized concentration-time curve, (e) deformation gradient-time curve, (f) the concentration map of the particles at 7000s, and (g) the mises map of the jellyroll and battery casing at 7000s.

Then, the extra dimension nodes method is implemented in COMSOL via weak form. By introducing a test function $\hat{c}_s$, The weak form of Eq. (16) can be thus expressed as

$$\int_r \left(\frac{\partial c_s}{\partial t}+\frac{1}{r^2}\frac{\partial r^2 j_s}{\partial r}\right)\hat{c}_s dr=0 \tag{17}$$

according to Eqs. 12–14, j_s can be expressed as

$$j_s=A\frac{\partial c_s}{\partial r}+B\frac{\partial \sigma_h}{\partial r} \tag{18}$$

where

$$A=\frac{D_0F}{RT}\left(\frac{c_s}{c_{s,\max}}\right)(c_{s,\max}-c_s)\frac{\partial E_{ref}}{\partial c_s}, \tag{19}$$

$$B=\frac{D_0F}{RT}\left(\frac{c_s}{c_{s,\max}}\right)(c_{s,\max}-c_s)\Omega. \tag{20}$$

The P1 can be regarded as a C-core and Si-shell structure such that the weak form (Eq. (17)) can be expressed as

$$\int_0^{r_C} r^2\left(-\frac{\partial c_{s,C}}{\partial t}\hat{c}_{s,C}+j_{s,C}\frac{\partial \hat{c}_{s,C}}{\partial r}\right)dr=r^2\hat{c}_{s,C}j_{s,C}\Big|_0^{r_c} \tag{21}$$

$$\int_{r_C}^{r_p} r^2\left(-\frac{\partial c_{s,Si}}{\partial t}\hat{c}_{s,Si}+j_{s,Si}\frac{\partial \hat{c}_{s,Si}}{\partial r}\right)dr=r^2\hat{c}_{s,Si}j_{s,Si}\Big|_{r_C}^{r_p} \tag{22}$$

with the subscript "C" for graphite-core and subscript "Si" for Si-shell. For example $c_{s,C}$ and $c_{s,Si}$ are the Li concertation for C-core and Silicon-shell in solid-phase separately. The initial conditions and the boundary conditions are

$$\begin{aligned}&\mu_C=\mu_{Si} \quad \text{at} \quad r=r_C.\\ &j_{s,C}=-j_{s,Si} \quad \text{at} \quad r=r_C\end{aligned} \tag{23}$$

$$\frac{\partial c_{s,C}}{\partial r}=0 \quad \text{at} \quad r=0, \tag{24}$$

$$j_{s,Si}=\frac{i_{\mathrm{P1}}}{F} \quad \text{at} \quad r=r_p, \tag{25}$$

$$c_s(r)=c_{s0} \quad \text{at} \quad t=0. \tag{26}$$

where i_1 is from Eq. (1) and c_{s0} is the initial Li concentration in C and Si, respectively. The hydrostatic stress σ_h can be computed through the following governing equations and boundary conditions as follows

$$\frac{d\sigma_r}{dr}+\frac{2}{r}(\sigma_r-\sigma_\theta)=0. \tag{27}$$

$$u_{r,C} \quad \text{is bounded} \quad \text{at} \quad r=0, \tag{28}$$

$$\begin{aligned}&u_{r,Si}=u_{r,C} \quad \text{at} \quad r=r_C,\\ &\sigma_{h,Si}=\sigma_{h,C} \quad \text{at} \quad r=r_C\end{aligned} \tag{29}$$

$$u_{r,Si}=\left(\sqrt[3]{\det\mathbf{F}_{P1}}-1\right)r_p \quad \text{at} \quad r=r_p. \tag{30}$$

where the $\det\mathbf{F}_{P1}$ can be computed by the homogenized mechanical model, which will be introduced in the next section.

Similarly, considering the simpler structure of P2, the weak form and the boundary conditions of P2 can be expressed as

Table 3
Material and geometry parameters used in the model for validation.

Parameters	Value	Reference
Battery model		
H_{ca}	58.5 μm	Measured
H_{an}	49 μm	Measured
H_{sep}	8 μm	Measured
S_{1D}	0.121 m^2	Measured
$E_{ref}(c_{s,Si/C/LiCoO_2})$	Fig. 5(a)	[9,33]
$\varepsilon_{s,ca}$	0.58	Estimated
$\varepsilon_{e,ca}$	0.23	Estimated
$\varepsilon_{s,an}$	0.59	Estimated
$\varepsilon_{e,an}$	0.24	Estimated
$\kappa_{s,ca}$	100 S/m	[38]
$\kappa_{s,an}$	1 S/m	[39,40]
c_{e0}	1,000 mol/m^3	[41]
D_e	$7.5\times10^{-11} m^2/s$	[41]
κ_e	$f(c_e)$	[41]
t_+	0.363	[41]
$c_{s,\max,Si}$	278,000 mol/m^3	[39]
$c_{s,\max,C}$	36233 mol/m^3	Estimated
D_{Si}	$1.67\times10^{-14} m^2/s$	[42,43]
D_C	$5.5\times10^{-14} m^2/s$	[44]
$r_{p,an}$	5 μm	Estimated
$r_{p,ca}$	6 μm	Estimated
Ω_{Si}	$9\times10^{-6} m^3/mol$	[42]
Ω_C	$3.17\times10^{-6} m^3/mol$	[45]
Mechanical model		
E_{Si}	$E_{Si}(c_{s,Si})$	[46]
E_C	$19.25+82.23x$ Gpa	[45]
E_{ca}	182MPa	[47]
E_{an}	140MPa	[47]
E_{sep}	262MPa	[48]
E_{cas}	1.5 GPa	[9]
σ_j	$139.4\varepsilon^{1.406}$[MPa]	Measured
Battery size	84mm × 64mm × 3.4mm	Measured

$$\int_0^{r_p} r^2\left(-\frac{\partial c_{s,P2}}{\partial t}\widehat{c}_{s,P2}+j_{s,P2}\frac{\partial \widehat{c}_{s,P2}}{\partial r}\right)dr = r^2\widehat{c}_{s,P2}j_{s,P2}\Big|_0^{r_p} \tag{31}$$

$$\frac{\partial c_{s,P2}}{\partial r}=0 \quad \text{at} \quad r=0\,, \tag{32}$$

$$j_s=\frac{i_{P2}}{F} \quad \text{at} \quad r=r_p\,, \tag{33}$$

$$u_{r,P2} \quad \text{is bounded} \quad \text{at} \quad r=0\,, \tag{34}$$

$$u_{r,P2}=\left(\sqrt[3]{\det\mathbf{F}_{P2}}-1\right)r_p \quad \text{at} \quad r=r_p\,. \tag{35}$$

2.2.2. Homogenized mechanical model

The homogenized modeling method is used to describe the mechanical stress for computational efficiency without losing accuracy. The jellyroll (consisting of an anode, separator, and cathode) is treated as a homogeneous material. The uniaxial stress-strain model [3] is used for the constitutive model of the jellyroll as follows

$$\sigma=A\varepsilon^n+B \tag{36}$$

where σ is the stress and ε is the strain for the homogenized material. The parameters A and n can be determined through the compression experiment.

The deformation of the jellyroll is caused by the lithium intercalation/deintercalation of the anode and cathode, thus

$$\Delta V_{d,j}=\Delta V_{d,an}+\Delta V_{d,ca} \tag{37}$$

where $\Delta V_{d,an}$ and $\Delta V_{d,an}$ are the volume change of anode and cathode caused by diffusion induced deformation, respectively. The eigen strain caused by intercalation can be written as

$$\varepsilon_{eigen}=\sqrt[3]{\frac{\Delta V_d}{V}+1}=\alpha_{eff}(1+\Delta c_s) \tag{38}$$

where α_{eff} is the coefficient of lithiation expansion. Thus, the deformation of the cathode caused by diffusion induced deformation can be written as

$$\Delta V_{d,ca}/V_{ca}=\left(\alpha_{eff,ca}\left(1+\Delta c_{s,ca}\right)\right)^3-1 \tag{39}$$

Therefore, the total deformation can be expressed by considering deformations of P1 and P2, as

$$\begin{aligned}\Delta V_{d,an}/V_{an}=&\left(\left(\alpha_{eff,P2}\left(1+\Delta c_{s,P2}\right)\right)^3-1\right)\left(1-\gamma_{P1}\right)+\\&\left(\alpha_{eff,C}\left(1+\Delta c_{s,C}\right)\right)^3-1\right)\left(\gamma_{P1}-\gamma_{Si}\right)+\left(\left(\alpha_{eff,Si}\left(1+\Delta c_{s,Si}\right)\right)^3-1\right)\gamma_{Si}\end{aligned} \tag{40}$$

where γ_{P1} is the P1 ratio equals $\varepsilon_{s,P1}/\varepsilon_{s,an}$, and γ_{Si} is the Si ratio equals $\gamma_{Si/P1}\gamma_{P1}$(where $\gamma_{Si/P1}$ is the ratio of solid volume of Si to that of particle P1). The equivalent eigen strain of the jellyroll can then be estimated through Eqs. 37–40.

2.2.3. Coupling strategy

The average Li concentration of each component can be transported from the electrochemical model to the mechanical model. On the other hand, the deformation gradient $\det\mathbf{F}=(V+\Delta V)/V$ (where V is the initial volume and ΔV is the volume change) can be translated from the mechanical model to the battery model (Fig. 2).

$\det\mathbf{F}$ cannot be obtained directly from the mechanical homogenized model and should be obtained via.

$$\det\mathbf{F}=\det\mathbf{F}_e\det\mathbf{F}_d \tag{41}$$

$$V_j\det\mathbf{F}_{e,j}=V_{ca}\det\mathbf{F}_{e,ca}+V_{an}\det\mathbf{F}_{e,an}+V_{sep}\det\mathbf{F}_{e,sep} \tag{42}$$

$$\varepsilon_{e,ca}E_{ca}=\varepsilon_{e,an}E_{an}=\varepsilon_{e,sep}E_{sep} \tag{43}$$

where $\det\mathbf{F}_e$ and $\det\mathbf{F}_d$ are the deformation gradient of the elastic deformation and diffusion induced deformation.E_{ca}, E_{an}, E_{sep} are the elastic modulus. V_j, V_{ca}, V_{an} and V_{sep} are the volume of the jellyroll, cathode, anode, and separator. Considering graphite is the primary material of P1 ($\gamma_{Si/P1}$ is small). Thus deformation gradient is assumed the same for P1 and P2, i.e. $\det\mathbf{F}_{e,\ P1}=\det\mathbf{F}_{e,P2}=\det\mathbf{F}_{e,an}$.

2.3. Experiment setup

A commercial pouch cell ($LiCoO_2/Li_xC_6$) were used for model calibrating. The basic information of the battery is summarized in Table 2. Charging experiment and electrochemical impedance spectroscopy (EIS) testing at various mechanical loadings were designed to create mechanical-electrochemical coupled scenarios such as to study the stress-induced electrochemical behavior of LIB.

2.3.1. Charging experiment under various mechanical loadings

Batteries were first compressed quasi-statistically (loading speed at 0.05 mm/min) to a pre-set loading value (defined as initial loading below) based on INSTRON 2345 platform. Then the loading device remained still for 2 h to eliminate possible loading change caused by stress relaxation of the testing sample (shown in Fig. 3). The battery test device (BK-6808AR/5) was used to charge the battery at 0.5C constant current charge to 4.4 V and then constant voltage charge (at 1/50C). Note that to guarantee the equal initial electrochemical status before the

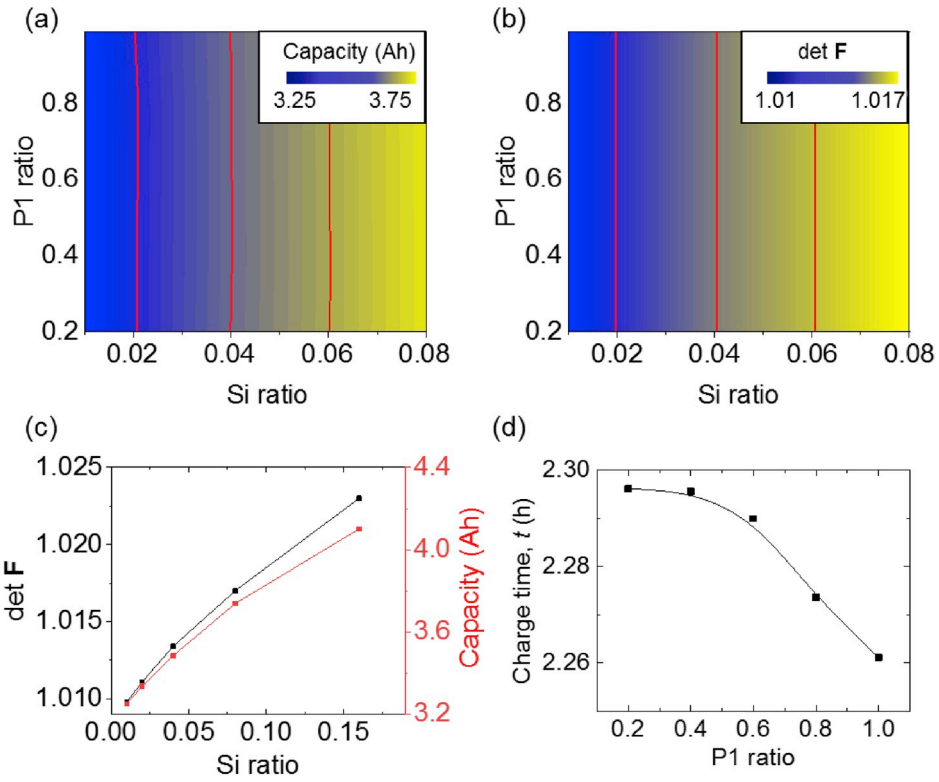

Fig. 6. (a) The charge capacity and (b) deformation gradient in different P1 ratio and Si ratio. (c) The relationship of the deformation gradient and Si ratio. (d) The relationship of charge time and P1 ratio.

experiment for all samples, batteries were charged fully and then discharged using 0.5 C rate to constant voltage discharge to 3 V by using 1/50C rate. Here, 1000 N and 2000 N were chosen as the initial loads. After 2 h for load holding, the measured load changed to 823 N and 1800 N, respectively.

2.3.2. EIS experiments at different mechanical loads

The EIS experiment (measured by potentiostat CHI 660) was operated at different initial loading conditions from 0 N–2000 N. The frequency for original EIS data was measured from 0.02 Hz to 10000 Hz. The measured battery was firstly discharged to 3 V at 0.5C constant current and then constant voltage at 1/50C constant current. The typical EIS result of this battery is composed of two partially overlapped semicircles and a straight line at low-frequency end, which can be fitted by an equivalent circuit shown in Fig. 4(a). The equivalent circuit model is composed of R_b (bulk resistance of the cell), R_{SEI} (resistance of the solid-state interface), C_{SEI} (capacitance of the solid-state interface, R_{ct} (faradaic charge-transfer resistance), C_{dl} (double-layer capacitance) and W_s (Warburg impedance). The parameters of the equivalent model can be fitted from the EIS experiment.

3. Results

3.1. Model validation

Based on the aforementioned governing equations and coupling strategy, one can have a fully coupled model describing the stress-induced electrochemical behavior and the expansion of LIB caused by Li-ion diffusion in multiscale with the consideration of the mixture of Si and graphite in microscale.

3.1.1. Validation of stress-induced behavior and expansion of LIB caused by diffusion

Here, a battery with pure graphite as an anode material is also modeled for a fair comparison. As such, $\varepsilon_{s,P1} = 0$. The numerical computation is based on COMSOL Multiphysics. The hexahedral mesh is used to describe the jellyroll 3D mechanical model with a total of 340 elements. The quadrilateral mesh is used to depict the battery casing while wire mesh is employed for the 1D battery model with the total element number is 44. Parameters are summarized in Table 3.

One may observe that both the voltage and load increase with the charging process. The voltage curve of the batteries under 2000 N is a little higher than the cells under 1000 N (about 5 mV differences, Fig. 4 (b)), demonstrating an evident influence from that mechanical stress over the electrochemical properties of the battery.

In the meantime, the fitting parameters of EIS experiments show that R_b and R_{sei} almost do not change with the increases of mechanical load/stress, where $R_b \approx 0.0329\ \Omega$ and $R_{sei} \approx 0.0054\ \Omega$. However, R_{ct} increases with the initial loading, which ranges from 0.116 Ω to 0.122 Ω with increasing of load (500 N–2000 N). Thus, mechanical stress has a nontrivial effect over the transfer and lithium diffusion related resistance (also evidenced by Eqs. (13) and (15)).

The maximum increased stress-induced force of the batteries (due to charging) would be 0.78 kN if the initial loading $F_{int} = 2000$ N while it would be 0.73 kN if the initial loading $F_{int} = 1000$ N. The responsible reason should be the expansion of battery due to Li diffusion (as expressed in Eqs. 37–43), and the tangent modulus of the cell becomes greater as strain increases (as shown in Eq. (36)).

The model shows good agreement of the experiments and the simulations both in voltage and the force profiles. Moreover, it is capable of predicting the slight differences in the voltage curve in different compression loadings, shown in Fig. 4(b). Results indicate that this model predicts the stress-induced behavior and expansion of LIB successfully.

3.1.2. Si/G mixture validation

The half cell (Si/G) experiment developed by Ref. [33] was adopted here for model validation. The structure of the Si/G composite particle

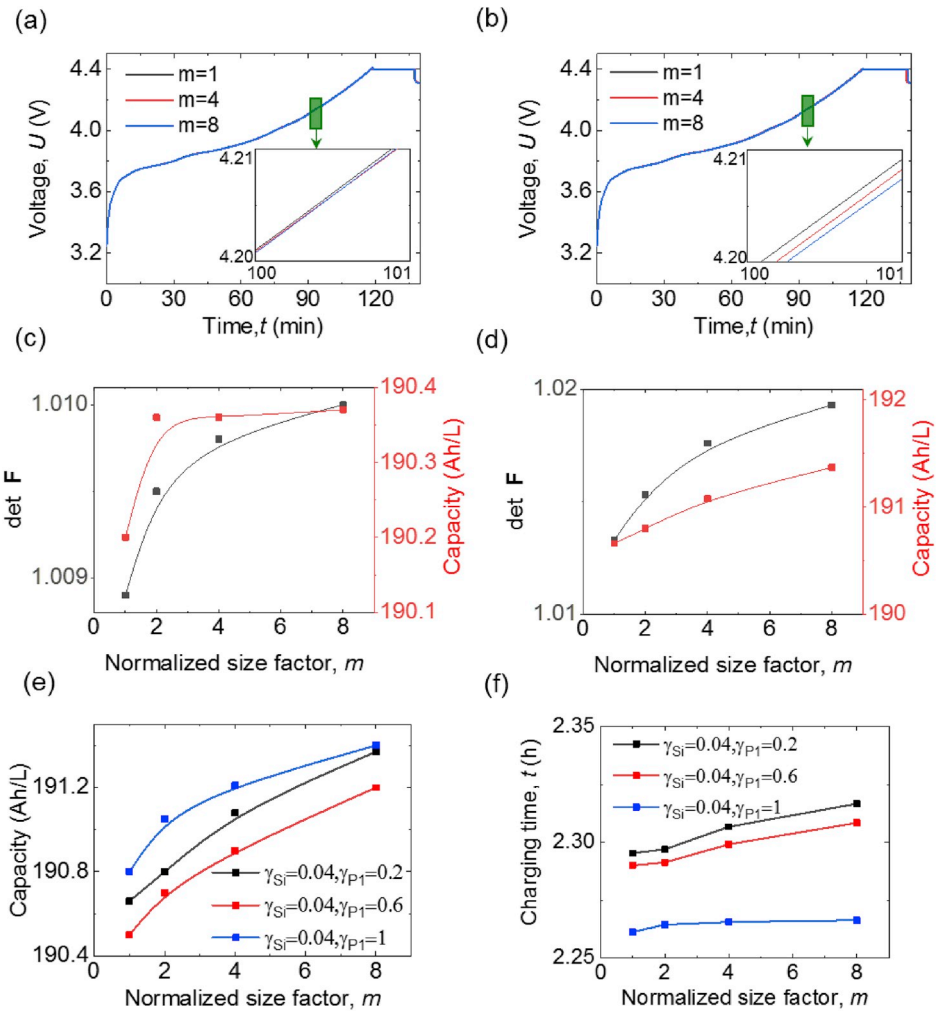

Fig. 7. The voltage-time curve in various battery sizes for (a) hard battery casing and (b) soft battery casing. The relationship of battery size, deformation gradient and charge capacity for (c) hard battery casing and (d) soft battery casing. (e) The relationship of capacity and battery size in different γ_{P1} (soft battery casing). (f) The relationship of charging time and battery size in different γ_{P1} (soft battery casing).

(P1) in Ref. [33] is shown in Fig. 1 (a). For validation purposes, The ratio of pure graphite particle P2 = 0. According to Ref. [33], the volume fraction of Si is set to be 4.1%. The results show good agreement with experiments, shown in Fig. 5(b), and thus the model is validated.

3.2. Typical computational results for the target model

Now it is safe to employ the validated model to study the electro-mechanical behavior of LIB with such anode material. The same size battery as described in Section 2.3 containing the anode (P1 ratio $\gamma_{P1} = \varepsilon_{s,P1}/\varepsilon_{s,an} = 0.2$ and Si ratio $\gamma_{Si} = \gamma_{Si/P1}\gamma_{P1} = 0.04$, where $\gamma_{Si/P1}$ is the Si ratio of P1) is computed using this model. Constant current charge (1.675 A) to constant voltage charge (to 0.1675 A) modes are applied for this battery.

For cathode wise, the normalized concentration of Li in the cathode ($c_s/c_{s,\max}$) decreases linearly because of constant current. However, for each component of the anode, the normalized concentration of Li increases nonlinearly because of the difference in open-circuit potentials between graphite and silicon. According to the curves in Fig. 5(d), during the constant current charge stage, the normalized Li concentration in Si is higher than that in graphite because the open circuit potential of Si is higher than graphite (shown in Fig. 5(a)). At the same time, the green line (Li concentration in graphite of P1) is higher than the blue line (Li concentration in graphite of P2). Such phenomenon is due to the boundary conditions of Li flux in the graphite of P2 governed by the intercalation at the solid/liquid interface (Eq. (1) and (2)) while the boundary conditions of Li flux in the graphite of P1 is governed by the Li flux exchange at the interphase of Si and graphite (Eq. (23)). The Li concentration gradient along the radius is minimal due to the slow charging rate (Fig. 5(f)). During the constant voltage charge stage, the Li concentration of graphite and Si in P1 both decrease slightly while Li concentration of graphite in P1 increases in this stage.

The trend of deformation gradient for P1 and P2 is similar to the trends of the Li concentration shown in Fig. 5(d) and (e). The detFof P1, P2, and the jellyroll after charging are 1.158, 1.029 and 1.013 separately. The maximum von mises stress of the battery casing and jellyroll are about 8 MPa and 0.4 MPa during charging, respectively (Fig. 5(g)). Stress is mostly concentrated within the vicinity of the battery casing corner, indicating a potential safety failure location.

4. Discussion

4.1. The effect of the mixture parameters of P1 and P2

There are two important design parameters in the model, i.e., γ_{Si} and γ_{P1} for various Si/G ratios. To guarantee a fair comparison, the maximum lithium content of the anode and cathode have the following relationship, that is

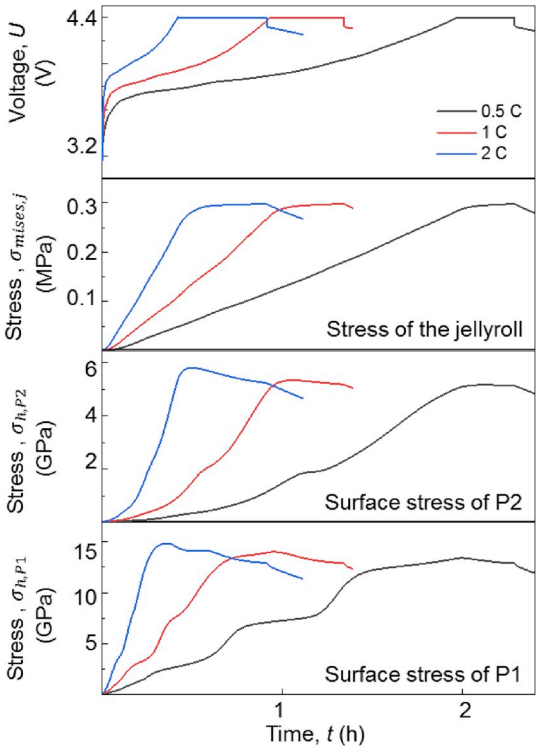

Fig. 8. (a) The voltage-, (b) Mises stress of the jellyroll-, (c) surface stress of P2- and (d) surface stress of P1-time curve in different charge rates.

$$c_{s,\max,ca} V_{ca} \varepsilon_{s,ca} = V_{an} \begin{pmatrix} c_{s,\max,C} S_{1D} L_{an} \varepsilon_s (1 - \gamma_{P1}) + c_{s,\max,Si} S_{1D} L_{an} \varepsilon_s \gamma_{Si} \\ + c_{s,\max,C} S_{1D} L_{an} \varepsilon_s (\gamma_{P1} - \gamma_{Si}) \end{pmatrix} (1 - \omega) \tag{44}$$

where ω is the design surplus of the anode electrode, and it is chosen as 0.05 here, according to the reasonable areal capacity ratio of negative to positive electrodes (N/P ratio) ranges [49,50].

The charging current is set as 1.675 A, and the cut-off current at the constant voltage is set as 0.1675 A. The capacities for all cases using this charging method are summarized in Fig. 6(a) in a color map. Results show the charging capacity almost remains the same with γ_{P1} but increases with γ_{Si}. Correspondingly, the maximum deformation gradient has a similar phenomenon with the charge capacity, shown in Fig. 6(b). Intuitively, both of deformation gradient and charge capacity increase nonlinearly with γ_{Si} (Fig. 6(c)). One may observe easily that it needs less time to charge fully for larger γ_{P1} (Fig. 6(d)). As such, the rate performance of the LIB can be improved through larger γ_{P1}.

4.2. The effect of the design parameters in the cell scale

Our previous study has shown that stiffness is an essential factor to influence the voltage behavior for small-sized batteries [30]. In the meantime, battery size may affect largely for the overall energy density for the battery pack. However, the previous model is not fit for the commercial batteries for the poor low computational efficiency. Using the present model, the battery sized were discussed with "soft" and "hard" battery casings. Here, two typical types of battery casings are chosen, i.e., soft casing and hard casing represented by materials of Young's modulus of 1.5 GPa [9] and 207 GPa [3], the thickness of 0.07 mm and 0.3 mm, respectively.

The baseline size of the battery is 84 mm × 64 mm × 3.4 mm. Here we use normalized size m to represent the size of the cell, and then the actual size of the battery becomes $84m$ mm × $64m$ mm × $3.4m$ mm. The charging method is the same as described in Section 3.2. Note that the thickness of the battery casing would not change with m.

For hard battery casing, the voltage of the battery is almost the same with various battery sizes (e.g. $m = 1, 4, 8$) (Fig. 7(a)). However, for the soft casing, the voltage is lower in larger sizes (Fig. 7(b)). Such a phenomenon is mainly due to a more drastic deformation gradient change for soft battery casing. The deformation gradient and charge capacity both increase with the size of the battery, and such a phenomenon becomes more prominent in soft casing batteries (Fig. 7(c) and (d)). The charge capacity increases with the size of the battery in various γ_{P1}. However, there is no obvious relationship of charge capacity and γ_{P1} at different battery sizes (Fig. 7(e)). The charging time increases with the increasing of battery size and decreasing of γ_{P1}. γ_{P1} has a more influencing effect e more than the battery sizes on the charging time (Fig. 7 (f)).

The results indicate that more mechanical constraints cause smaller deformation for the jellyroll and the deformation inhibition (internal stress) makes it more difficult to charge fully for the LIB. Therefore, a large battery size is recommended for battery pack design for Si/G based batteries for faster charging to a higher capacity.

Generally, electric vehicles have pressing needs for battery space and energy density. These two factors are, to a large extent, contradictories in design. Meanwhile, the deformation/stress of the Si-Graphite based battery during charging/discharging played an essential role in electrochemical performance. Thus, this model can assist the design for size and capacity for battery modules and packs and also provide fundamental models for monitoring battery pack safety.

4.3. The internal mechanical stress of LIB in different charge rate

The mechanical stress is produced during charging both in the microparticles and the jellyroll. Using the present model, the charge were discussed. 0.5 C, 1 C, and 2 C charge rate were chosen in this study, and the cut-off current at the constant voltage is set as 1/20 C for all charge rates.

Both of the maximum stress of the jellyroll ($\sigma_{mises,j,\max}$) and the particles ($\sigma_{h,P1,\max}$ and $\sigma_{h,P2,\max}$) are extracted from the results (shown in Fig. 8). The maximum value of $\sigma_{mises,j,\max}$ happens at the end of the constant voltage charge stage, and it changes little with the increase of charge rates. The maximum value of $\sigma_{mises,j,\max}$ (around 0.3 MPa) is much smaller than the internal short circuit (ISC) trigger stress (about 16 MPa [51]). Thus, ISC will not be triggered directly by the expansion for a fresh battery. The internal stress of the jellyroll should still be concerned for the cycled batteries. Because for a cycled battery, the thickness of solid electrolyte interphase and the lithium plating will produce extra expansion of LIB [52], and the coupling effect of them may cause safety problems. The deformation caused by SEI and lithium plating will be considered in our future studies.

The position of $\sigma_{h,P2,\max}$ and $\sigma_{h,P1,\max}$ at surface of the particles close to the separator and the maximum value of it happens during the constant voltage charge stage (the maximum value of $\sigma_{h,P2,\max}$ happens earlier than $\sigma_{h,P1,\max}$). Both of the maximum value of $\sigma_{h,P1,\max}$ and $\sigma_{h,P2,\max}$ increases with the increasing of charge rate. The crack of the particles is often caused by mechanical stress [53]. Thus, the maximum value of $\sigma_{h,P1,\max}$ and $\sigma_{h,P2,\max}$ should be carefully controlled within the failure threshold. Using the present model, one may easily control the maximum value of $\sigma_{h,P1,\max}$ and $\sigma_{h,P2,\max}$ through reasonable design parameters, mechanical boundary conditions and charging methods.

5. Concluding remarks

In this study, a computational model framework for lithium-ion battery with Si/G composite anode was established through the coupling of a stress-induced electrochemical model and homogenized mechanical model. For the electrochemical model, both the structures of the particles and the stress effect were considered by modifying the classical P2D model. In the meantime, nonlinear mechanical properties

of the jellyroll and the expansion caused by Li diffusion were both included in the homogenized mechanical model. The average deformation gradient of the mechanical model and the average concentrations of the battery model were transferred to couple each other. The multiphysical coupling model and the related parameters were then validated by mechanically loaded charging experiments for Si/G component anode. Further, parametric studies for governing factors (e.g., the Si/G mixture ratio and battery size) are discussed from a designing perspective. Results provide a powerful tool for Si/G composite anode design for a better electrochemical performance and understanding of fundamental failure mechanism of composite anode, paving a robust way for future high energy density battery cell, pack and module design, monitoring and evaluation for broad application of electric vehicles and 3C products (computers, cellphones and communication devices).

Author contribution

J.X. and B.L. conceived the study. B.L., and Y. J. conducted the experiment and established FE model. B.L., Y. J., H. J., S. Y. and J.X. analyzed the data. B. L., J.X., H. J. and S. Y. wrote the manuscript.

Declaration of competing interest

There are no conflicts to declare.

Acknowledgment

B. L. and S. Y. would like to thank the financial support by The National Key Research and Development Program of China (2017YFB0103703). B. L. would like to thank the financial support by The National Science Foundation of China (11902022), China Postdoctoral Science Foundation (2019M650439 and 2019TQ0017), and Opening Fund of Key Laboratory of Impact and Safety Engineering (Ningbo University), Ministry of Education (cj201907). H. J. acknowledges the support from the National Science Foundation under Grant No. CMMI-1929806.

References

[1] P. Li, G. Zhao, X. Zheng, X. Xu, C. Yao, W. Sun, S.X. Dou, Energy Storage Mater. 15 (2018) 422–446.
[2] L. Wang, S. Yin, J. Xu, J. Power Sources 413 (2019) 284–292.
[3] J. Xu, B. Liu, X. Wang, D. Hu, Appl. Energy 172 (2016) 180–189.
[4] L. Greve, C. Fehrenbach, J. Power Sources 214 (2012) 377–385.
[5] E. Sahraei, R. Hill, T. Wierzbicki, J. Power Sources 201 (2012) 307–321.
[6] B. Liu, Y. Jia, C. Yuan, L. Wang, X. Gao, S. Yin, J. Xu, Energy Storage Mater. 24 (2020) 85–112.
[7] B. Liu, S. Yin, J. Xu, Appl. Energy 183 (2016) 278–289.
[8] B. Liu, H. Zhao, H. Yu, J. Li, J. Xu, Electrochim. Acta (256) (2017) 172–184.
[9] B. Liu, Y. Jia, J. Li, S. Yin, C. Yuan, Z. Hu, L. Wang, Y. Li, J. Xu, J. Mater. Chem. 6 (2018) 21475–21484.
[10] M. Astaneh, R. Dufo-López, R. Roshandel, F. Golzar, J.L. Bernal-Agustín, J. Energy Storage 17 (2018) 93–101.
[11] S. Santhanagopalan, Q. Guo, P. Ramadass, R.E. White, J. Power Sources 156 (2006) 620–628.
[12] Z. Deng, L. Yang, H. Deng, Y. Cai, D. Li, Energy 142 (2018) 838–850.
[13] K. Zhao, M. Pharr, S. Cai, J.J. Vlassak, Z. Suo, J. Am. Ceram. Soc. 94 (2011) s226–s235.
[14] A.F. Bower, P. Guduru, Model. Simul. Mater. Sci. Eng. 20 (2012), 045004.
[15] R.T. Purkayastha, R.M. McMeeking, Comput. Mech. 50 (2012) 209–227.
[16] A.F. Bower, P.R. Guduru, V.A. Sethuraman, J. Mech. Phys. Solids 59 (2011) 804–828.
[17] Y. Gwak, J. Moon, M. Cho, J. Power Sources 307 (2016) 856–865.
[18] E. Jacques, M.H. Kjell, D. Zenkert, G. Lindbergh, Carbon 68 (2014) 725–733.
[19] D. Bresser, K. Hosoi, D. Howell, H. Li, H. Zeisel, K. Amine, S. Passerini, J. Power Sources 382 (2018) 176–178.
[20] W.J. Mai, A. Colclasure, K. Smith, J. Electrochem. Soc. 166 (2019) A1330–A1339.
[21] B. Lu, Y. Song, Q. Zhang, J. Pan, Y.-T. Cheng, J. Zhang, Phys. Chem. Chem. Phys. 18 (2016) 4721–4727.
[22] H. Yang, F. Fan, W. Liang, X. Guo, T. Zhu, S. Zhang, J. Mech. Phys. Solids 70 (2014) 349–361.
[23] C.V. Di Leo, E. Rejovitzky, L. Anand, J. Mech. Phys. Solids 70 (2014) 1–29.
[24] S. Huang, F. Fan, J. Li, S. Zhang, T. Zhu, Acta Mater. 61 (2013) 4354–4364.
[25] R. Grantab, V.B. Shenoy, J. Electrochem. Soc. 159 (2012) A584–A591.
[26] I. Ryu, S.W. Lee, H. Gao, Y. Cui, W.D. Nix, J. Power Sources 255 (2014) 274–282.
[27] X. Gao, P. He, J. Ren, J. Xu, Energy Storage Mater. 18 (2019) 23–33.
[28] H. Mendoza, S.A. Roberts, V.E. Brunini, A.M. Grillet, Electrochim. Acta 190 (2016) 1–15.
[29] S. Kim, J. Wee, K. Peters, H.Y.S. Huang, J. Phys. Chem. C 122 (2018) 5280–5290.
[30] B. Liu, X. Wang, H.-S. Chen, S. Chen, H. Yang, J. Xu, H. Jiang, D.-N. Fang, J Appl. Mech. Trans. ASME 86 (2019), 041005.
[31] W. Wu, X. Xiao, X. Huang, S. Yan, Comput. Mater. Sci. 83 (2014) 127–136.
[32] K.-Y. Oh, B.I. Epureanu, J.B. Siegel, A.G. Stefanopoulou, J. Power Sources 310 (2016) 118–129.
[33] F.-S. Li, Y.-S. Wu, J. Chou, N.-L. Wu, Chem. Commun. 51 (2015) 8429–8431.
[34] S. Jeong, X. Li, J. Zheng, P. Yan, R. Cao, H.J. Jung, C. Wang, J. Liu, J.-G. Zhang, J. Power Sources 329 (2016) 323–329.
[35] N. Kim, S. Chae, J. Ma, M. Ko, J. Cho, Nat. Commun. 8 (2017).
[36] W. Liu, Y.M. Zhong, S.Y. Yang, S.S. Zhang, X.Y. Yu, H.Q. Wang, Q.Y. Li, J. Li, X. Cai, Y.P. Fang, Sustain. Energy Fuels 2 (2018) 679–687.
[37] Q. Xu, J.-Y. Li, J.-K. Sun, Y.-X. Yin, L.-J. Wan, Y.-G. Guo, Adv. Energy Mater. 7 (2017).
[38] W.D. Zheng, M. Shui, J. Shu, S. Gao, D. Xu, L.L. Chen, L. Feng, Y.L. Ren, Bull. Mater. Sci. 36 (2013) 495–498.
[39] V.A. Sethuraman, V. Srinivasan, J. Newman, J. Electrochem. Soc. 160 (2013) A394–A403.
[40] V. Srinivasan, J. Newman, J. Electrochem. Soc. 151 (2004) A1530–A1538.
[41] M. Doyle, J. Newman, A.S. Gozdz, C.N. Schmutz, J.M. Tarascon, J. Electrochem. Soc. 143 (1996) 1890–1903.
[42] M. Wang, X. Xiao, X. Huang, J. Power Sources 307 (2016) 77–85.
[43] P. Johari, Y. Qi, V.B. Shenoy, Nano Lett. 11 (2011) 5494–5500.
[44] M. Park, X.C. Zhang, M.D. Chung, G.B. Less, A.M. Sastry, J. Power Sources 195 (2010) 7904–7929.
[45] Y. Qi, H.B. Guo, L.G. Hector, A. Timmons, J. Electrochem. Soc. 157 (2010) A558–A566.
[46] X. Wang, S.S. Singh, T. Ma, C. Lv, N. Chawla, H.Q. Jiang, Chem. Mater. 29 (2017) 5831–5840.
[47] J. Xu, B. Liu, D. Hu, Sci. Rep. (UK) 6 (2016) 21829.
[48] J. Xu, L.B. Wang, J. Guan, S. Yin, Mater. Des. 95 (2016) 319–328.
[49] C.-S. Kim, K.M. Jeong, K. Kim, C.-W. Yi, Electrochim. Acta 155 (2015) 431–436.
[50] Y. Abe, S. Kumagai, J. Energy Storage 19 (2018) 96–102.
[51] J. Xu, B. Liu, L. Wang, S. Shang, Eng. Fail. Anal. 53 (2015) 97–110.
[52] X.-G. Yang, Y. Leng, G. Zhang, S. Ge, C.-Y. Wang, J. Power Sources 360 (2017) 28–40.
[53] M. Klinsmann, D. Rosato, M. Kamlah, R.M. McMeeking, J. Mech. Phys. Solids 92 (2016) 313–344.